

Universally stable microresonator Turing pattern formation for coherent high-power THz radiation on-chip

Shu-Wei Huang^{1,*}, Jinghui Yang¹, Shang-Hua Yang², Mingbin Yu³, Dim-Lee Kwong³, T. Zelevinsky⁴, Mona Jarrahi², and Chee Wei Wong^{1,*}

¹ Fang Lu Mesoscopic Optics and Quantum Electronics Laboratory, University of California, Los Angeles, CA 90095, USA.

² Terahertz Electronics Laboratory, University of California, Los Angeles, CA 90095, USA.

³ Institute of Microelectronics, A*STAR, Singapore 117865, Singapore.

⁴ Department of Physics, Columbia University, New York, NY 10027, USA.

* Author e-mail address: swhuang@seas.ucla.edu ; cheewei.wong@ucla.edu

The spontaneous breaking of symmetry and homogeneity through dissipative self-organized Turing pattern formation is a fundamental question in developmental biology, molecular biochemistry, mathematics and nonlinear physics. In nonlinear microresonators driven by continuous-wave lasers, Turing structures have been observed experimentally and studied in the formalism of Lugiato-Lefever equation. Destabilization of Turing pattern and transition to spatio-temporal chaos, however, limits the available energy carried in the Turing rolls and prevents further harvest of their high coherence and robustness to noise. Here we report the universally stable microresonator Turing pattern formation in chip-scale nonlinear oscillators, obtaining a record high conversion efficiency of 45% and an elevated spectral asymmetry. Local mode hybridizations are purposefully introduced in the nonlinear microresonator to seed the coherent pattern formation and circumvent the Turing pattern destabilization. The stationary Turing pattern is discretely tunable across 430 GHz on a THz carrier, with a fractional frequency sideband non-uniformity measured at 6.6×10^{-16} . We demonstrate the simultaneous microwave and optical coherence of the Turing rolls at different evolution stages through ultrafast optical correlation techniques. The free-running Turing roll coherence, 9 kHz in 200 ms and 160 kHz in 20 minutes, is transferred onto a plasmonic photomixer for one of the highest power THz coherent generation at room-temperature, with 1.1% optical-to-THz power conversion and applications in astrophysics, imaging, sensing, and wireless communications.

The spontaneous formation of stationary periodic patterns from instability and a homogenous background examined by Turing has served as the basis for developmental biology morphogenesis, chemical kinetics far-from-equilibrium, and the formation of fractals and chaos in nonlinear dynamics [1-3]. When driven above threshold, these patterns can be robust against perturbations, even with noisy initial conditions. The Turing model universally casts the complexity of these spontaneous self-organized patterns into nonlinear reaction kinetics and diffusion characteristics, or equivalently in optics, the nonlinear Kerr medium and group velocity dispersion (GVD) from space-time duality. In optical systems, Lugiato and Lefever first theoretically proposed the symmetry-breaking instabilities [4] that lead to the spontaneous formation of stationary Turing patterns. These dissipative structures arise from nonlinear microresonators, generally with anomalous GVD for convenient phase matching fulfillment, and can be described by super- and sub-critical regimes with stable and unstable pattern formations [5-7]. In the formation route of these spontaneous patterns (Figures 1a and 1b), other nonlinear dynamical states also exist such as breather states, spatiotemporal chaos [8, 9], solitons, and soliton molecules [10-14]. We note that the Turing roll, despite its optimally coherent properties [15], only exists in a limited phase space in this dispersion regime. As the driving laser is frequency tuned closer to the cavity resonance, the stable Turing rolls first collapse into breather states, then destabilize into spatio-temporal chaos, and eventually transitions into soliton molecules [16-18] or Kerr frequency comb [19-21]. Such destabilization thus limits the available energy carried in the stable Turing rolls and prevents further harvest of their high coherence and robustness to noise (Figure 1c).

To expand the stability zone and attain higher pump-to-comb conversion, we approach the spontaneous Turing pattern formation in a distinctly different way. Our Kerr nonlinear oscillator is designed to possess a large globally normal GVD of $100 \text{ fs}^2/\text{mm}$ (Figure 1d) and thus self organization is strictly forbidden unless local dispersion anomalies are introduced to the system, providing additional GVD to balance the nonlinearity locally. In our high Q oscillator (loaded quality factor of 3.7×10^5), such anomalies result from the hybridization of two transverse modes (TM_{11} and TM_{21}) with distinct free spectral ranges (FSRs) when their resonant frequencies are in the vicinity of each other [22-25]. The spectral position of the mode hybridization defines the Turing pattern formation dynamics and it can be changed by the design of the FSR difference. As the balance between the GVD and the Kerr nonlinearity is only fulfilled locally in the

confined spectral range where mode hybridization occurs, sub-comb growth and subsequent destabilization of the Turing pattern is avoided (Figure S1). By enabling the deeper driving-into-resonance without transition into chaos or soliton states, the conversion efficiency from pump to Turing pattern can thus be significantly enhanced in our system. The mode hybridization mediated phase matching – by adjusting the relative frequency between the pump mode and the mode hybridization position – further enables the repetition rate of the Turing roll to be discretely tunable. Moreover, the Turing roll spectra can exhibit controllable asymmetry (Figure S1) through registering the pump mode on different sides of the first local-mode hybridization region ε_1 (Figure 2a top row).

Here we report the universally stable microresonator Turing patterns in chip-scale nonlinear nitride cavities, with a broadband tunability from 1.14 THz to 1.57 THz and a record high power conversion of 45%. We utilize the mode hybridization mediated phase matching to obtain the broadband tunability and overcome the destabilization of Turing pattern, thereby achieving unprecedented pump depletion and record high power conversion. Symmetry breaking of the Turing roll spectra is also observed. We interrogate the commensurate and coherent nature of the spontaneous dissipative structure with ultrafast optical intensity autocorrelation, microwave spectral noise analysis, and heterodyne beating against a benchmark fiber frequency comb. The fractional frequency sideband non-uniformity of the nitride Turing pattern is measured at 6.6×10^{-16} , with a short-term (200 ms sweep time) linewidth of 9 kHz and a long-term (over 20 minutes) drift of 160 kHz. Towards THz applications, we then transfer the free-running Turing pattern coherence to a plasmonic ErAs:InGaAs photomixer, generating up to 600 μ W THz radiation power at room temperature. The demonstrated comb-THz system offers the potential to be the room temperature on-chip THz local oscillator for astrophysics, medical imaging, atmospheric sensing, and wireless communication [26-30].

Figure 2a shows the measured spectra of the spontaneous Turing patterns generated from ring resonators with different radii, with the pump illustrated in blue and the mode hybridization positions labeled as red dashed lines ε_1 . Despite very similar GVD β_2 from different radii ring resonators, the Turing patterns show spectral shapes distinct from each other. Specifically the spectral lines on the side of the first mode hybridization position are suppressed due to the increasing phase mismatch associated with the mode hybridization induced local dispersion disruption. With the first sideband pair ($m = \pm 1$) phase matched because of additional

contribution from the mode hybridization on mode 1, then the phase matching condition can be written as:

$$\Delta k(2\omega_0 - \omega_1 - \omega_{-1}) = \beta_2 \Delta^2 + \gamma P_{int} - \varepsilon = 0 ,$$

where ε represents the contribution from the mode hybridization, Δ the Turing roll repetition rate, γ the nonlinear Kerr coefficient, and P_{int} the intracavity power. Here $k_1 = k_0 + \beta' \Delta + \frac{\beta_2}{2} \Delta^2 + \varepsilon$, and $k_m = k_0 + \beta'(m\Delta) + \frac{\beta_2}{2} (m\Delta)^2$, where β' is the group velocity. Then the phase matching condition for the first cascaded FWM on *either* side of the pump can be written as:

$$\Delta k(2\omega_1 - \omega_2 - \omega_0) = \beta_2 \Delta^2 + \gamma P_{int} + 2\varepsilon = 3\varepsilon$$

$$\Delta k(2\omega_{-1} - \omega_0 - \omega_{-2}) = \beta_2 \Delta^2 + \gamma P_{int} = \varepsilon .$$

The phase mismatch on the side of the mode crossing position is three times larger than the other process and thus the symmetry of the Turing roll spectra is broken. Turing roll repetition rates also show dramatic variations, ≈ 640 GHz in the 180 μm radius ring and ≈ 1.72 THz in the 160 μm and 200 μm rings, that cannot be solely explained by the change in the cavity round-trip time. These features are direct consequences of the unique phase matching configuration employed in our design, with critical roles in the efficient coherence transfer from Turing pattern to THz radiation to be detailed subsequently.

Next we focus on the results generated from the 160 μm radius ring because of its energy concentration in the wavelength range shorter than 1570 nm. Figure 2b and 2c shows the pump and total transmitted intensities, measured simultaneously for different detunings. The pump transmission shows a triangular tuning curve with a strong dip from normalized unity into $\approx 10\%$ of the original transmission, while total transmission shows only a small drop from 48% to 41% – this supports the efficient total energy transfer from the pump into the complete Turing pattern sidebands. To examine this further, Figure 2d plots the corresponding Turing roll spectra at different detuning stages: stable spontaneous Turing pattern are observed without any sign of destabilization at all detunings. The power conversion efficiency, the integrated power of the Turing roll divided by the on-chip pump power, reaches as high as 45% at both stage II and III. Closer to resonance at the stage V, an even stronger pump depletion is achieved, with the pump intensity 2-dB lower than even the first modulation sidebands.

We conduct a series of ultrafast optical intensity autocorrelation (IAC) measurements, as shown in Figure 3a, to investigate the temporal structure of the Turing patterns at different

evolving stages. At all the stages, stable and strong quasi-sinusoidal oscillations are each observed. While pumping closer to resonance results in monotonic increase in the pump depletion (Figure 2d), counterintuitively the IAC traces show a discernible minimum background between stage II and stage III. At stage III, a peak-to-valley intensity contrast ratio of more than 100 is achieved (Figure S2). We next perform extensive measurements to examine the coherence of the spontaneous Turing formation, illustrated in Figure 3b to 3e. The RF amplitude noise spectra of the Turing pattern up to 3 GHz, six times the cavity linewidth, shows an absence of RF peaks and a noise level at the instrumentation detection background limit, indicative of the existence of a single Turing roll family with commensurate repetition rates (Figure 3b).

We further heterodyne beat the Turing comb lines ($m = \pm 1$ and pump) against a benchmark fiber frequency comb (Menlo FC1500-250-WG; see Appendix) and performed ratio counting of the sidebands to interrogate the frequency uniformity, which sets the fundamental limit on the coherence transfer from the Turing pattern (Figure 3c). When the Turing roll repetition rate is made non-divisible by the fiber frequency comb spacing, the beat frequencies of consecutive sidebands will be an arithmetic sequence. Namely, $\delta_2 = \delta_1 + \Delta = \delta_0 + 2\Delta$. Here we make the common difference, Δ , to be 1 MHz. Ideally, the ratio between $\delta_2 - \delta_0$ and $\delta_1 - \delta_0$, R , should be 2 and deviation from this ratio, ε_R , is a measure of the sideband frequency non-uniformity, $\varepsilon = \varepsilon_R \cdot \Delta$. Excellent sideband uniformity of the Turing pattern is observed at all evolving stages with the average non-uniformity measured at 125 mHz, or 6.6×10^{-16} when referenced to the optical carrier (Figure 3c).

Figure 3d next shows the delayed self-heterodyne beat note of the first sideband (see Appendix), demonstrating the Turing lines down to a pump-coherence-limited linewidth of 500 kHz. The linewidth measurements independently confirm the good coherence of the Turing rolls at all detunings. Figure 3e also shows the real-time power monitoring of the four strongest sidebands. All sidebands present similar intensity noise of less than 1% (integrated from 100 Hz to 100 MHz) and no cyclic energy exchange between sidebands is observed, excluding the possibility of breathing dynamics with conserved total power and supporting the evidence of stationary Turing pattern formation with extensive stability zone.

To examine whether the temporal shape of the spontaneous Turing pattern is subjected to the perturbation in the initial condition and the pump detuning scan, we performed the IAC measurements at three different tuning speeds and two independent starts. Each of the Turing

IAC dynamics remains identical to each other (Figure S3), illustrating the good robustness of the Turing patterns. To understand the dynamics better, ideal IAC traces from transform-limited Turing patterns are superimposed onto the measured IAC traces (Figure 3a; in red). As the Turing pattern is driven closer to resonance, there is increasing discrepancy of the measured pattern from the transform-limit. The change of temporal shapes without the coherence loss implies that the spectral phase of the Turing pattern varies at the different evolving stages and thus different external phase compensation strategies are necessary if the temporal properties of the Turing pattern are to be fully utilized. The spectral phase variation can be understood as the consequence of the pump phase slip around the resonance. The relationship between the output and the intracavity pump power can be written as:

$$A_{p,out} = -\frac{\gamma_c - \gamma_a - i\delta}{\sqrt{2}\gamma_c} \sqrt{T_R} A_{p,cav} ,$$

where γ_c and γ_a are the half-width half-maximum linewidths associated with the coupling losses and the intrinsic cavity losses respectively. In our microresonator, $\gamma_c = 160$ MHz and $\gamma_a = 90$ MHz. The output pump will experience a π phase shift as it traverses through the resonance (Figure S5a). Such phase slip is due to the interference between the intracavity and the input pump and thus the other sidebands of the Turing roll will not experience such a phase shift. This additional pump phase slip results in the observed change of temporal structure. The distinct responses to dispersion (illustrated in Figure S4; aiding between different Turing states) are well captured by considering the pump phase offset (Figure S5b). Of note, most of the phase slip happens very close to cavity resonance and thus the observation of its effect is attributed to the unique design of our microresonator, which utilizes the local mode hybridization to fulfill the phase matching of spontaneous Turing pattern formation and greatly suppresses the Turing pattern destabilization even when the pump is deep into the resonance.

The robustness, tunability, good coherence, and high efficiency of the demonstrated Turing roll make it an excellent photomixer pump for narrow linewidth tunable THz radiation. Different from deriving the pump from a mode-locked laser [30], the Turing comb pattern offers the advantage of efficient power use and reduced system complexity as its quasi-sinusoidal intensity profile (Figure S2) is directly applicable as a photomixer pump. Furthermore, using two independently-offset continuous-wave lasers does not permit stable efficient optical-to-THz conversion and sacrifices good long-term coherence in the THz radiation. To characterize the stability of the free-running Turing roll repetition rate, which determines the linewidth and drift

of the THz radiation, we beat the pump and one of the sideband with the adjacent fiber laser frequency comb lines and electrically mix the two signals to get the beat note at the frequency difference as shown in Figure 4a. Figure 4b shows the linewidth of the beat note with a sweep time of 200 ms, measuring a narrow FWHM linewidth of 9 kHz. Figure 4c shows the long term frequency drift, measuring a root-mean-square frequency fluctuation of 160 kHz over 20 minutes.

To convert the Turing pattern into the THz radiation, we fabricate an ErAs:InGaAs plasmonic photomixer (Figure 5a) which features a good spectral response from 0.8 to 1.6 THz due to the logarithmic spiral antenna design [31]. A C/L WDM filter, followed by an erbium doped fiber amplifier (EDFA), is used to selectively amplify the Turing pattern sidebands in the 1530 to 1565 nm C-band range. Of note, the EDFA is necessary only because our current Si₃N₄ microresonator has a strong *Q*-factor roll-off in C-band and thus we are limited to pump it in the L-band. Figure 4b shows four examples illustrating the tunability of the Turing roll repetition rate (1.14 to 1.57 THz), which in turn determines the THz frequency, by tuning the chip temperature or the pump wavelength. Figure 4c plots the room-temperature radiated THz power as a function of the optical pump power, showing a nearly quadratic dependence even at the maximum available pump power of 54 mW, without much saturation roll-off in the THz generation. Up to 600 μ W THz radiation power is generated with an optical-to-THz power conversion efficiency of 1.1%.

In summary, we report the observation of a highly efficient spontaneous Turing pattern formation with up to 45% power conversion. The record high conversion efficiency is achieved by expanding the Turing roll stability zone via designs of mode hybridization mediated phase matching in the chip-scale nitride nonlinear oscillator. Symmetry breaking of Turing roll spectrum is also observed. The Turing pattern sideband frequency non-uniformity is measured down to 6.6×10^{-16} . Furthermore, we show the free-running repetition rate of the Turing roll is discretely tunable across 430 GHz, with a short-term linewidth of 9 kHz (200 ms sweep time) and a long-term drift of 160 kHz (over 20 minutes). We demonstrate the temporal shapes of the Turing patterns change with respect to pump detuning, not because of the coherence loss but the pump phase slip near the cavity resonance. The robustness, tunability, good coherence, and high efficiency of the demonstrated Turing pattern make it an excellent photomixer pump for narrow linewidth tunable THz radiation. Pumping a novel ErAs:InGaAs plasmonic photomixer, we

generate up to 600 μW THz radiation power at room-temperature. With its high THz radiation power, large frequency tuning range, narrow short-term linewidth, and small long-term frequency drift, the demonstrated system offers the potential to be the room temperature on-chip THz local oscillator for astrophysics, medical imaging, atmospheric sensing, and wireless communication.

Acknowledgements: The authors thank discussions with Bart McGuyer. The authors acknowledge funding support from ONR (N00014-14-1-0041), AFOSR Young Investigator Award (FA9550-15-1-0081), DARPA (HR0011-15-2-0014), and NIST Precision Measurement Grant (60NANB13D163).

Appendix A: Si_3N_4 Turing microresonator fabrication

First a 3 μm thick oxide layer is deposited via plasma-enhanced chemical vapor deposition (PECVD) on *p*-type 8" silicon wafers to serve as the under-cladding oxide. Then low-pressure chemical vapor deposition (LPCVD) is used to deposit a 725 nm silicon nitride for the ring resonators, with a gas mixture of SiH_2Cl_2 and NH_3 . The resulting silicon nitride layer is patterned by optimized 248 nm deep-ultraviolet lithography and etched down to the buried oxide layer via optimized reactive ion dry etching. Next the silicon nitride ring resonators are over-cladded with a 3 μm thick oxide layer, deposited initially with LPCVD (500 nm) and then with PECVD (2500 nm). The propagation loss of the silicon nitride waveguide is measured to be 0.2 dB/cm at the pump wavelength. Precision characterization of the Turing resonator is through swept-wavelength interferometer and referenced against a hydrogen cyanide gas cell, and detailed in Supplemental Materials IV.

Appendix B: ultrafast optical intensity autocorrelation and self-heterodyne characterization

The optical intensity autocorrelator consists of a 1 mm thick β -BBO crystal, supporting a bandwidth of 200 nm, and a silicon avalanche photodiode, supporting a sensitivity of 100 μW . The setup is configured in a non-collinear geometry and careful checks are done before measurements to ensure only background-free second harmonic signals are collected. The use of dispersive optics is also minimized such that the additional dispersion introduced to the pulse is only -50 fs². To further confirm the coherence of the Turing lines, self-heterodyne linewidth measurements are performed with detailed setup shown in Supplemental Materials IV. With a 200 MHz acousto-optic modulator and 24.5 μs delay provided by a 5 km single mode optical

fiber, our self-heterodyne setup shows a minimum linewidth at 13 kHz, about 40 times smaller than the pump laser linewidth (≈ 500 kHz).

Appendix C: Turing pattern uniformity measurements against a fiber frequency comb

Sideband frequency uniformity of the Turing comb pattern is measured by heterodyne referencing against the benchmark optical fiber laser frequency comb, Menlo FC1500-250-WG. As detailed in Supplemental Materials IV, the spontaneous Turing roll is split into 3 beat detection units ($m = \pm 1$ and pump) with more than 40 dB signal to noise ratio at 100 kHz resolution bandwidth. The sideband beat notes (δ_1 and δ_2) were mixed with the pump beat note (δ_0) to cancel the residual pump wavelength instability, with the frequency counter operating in the ratio counting mode to circumvent synchronization of the simultaneous beat note measurements.

Appendix D: plasmonic photomixer fabrication

The plasmonic contact electrode gratings are designed to have 200 nm pitch, 100 nm metal width, 5/45 nm Ti/Au height, and 250 nm thick silicon nitride anti-reflection (AR) coating. They are patterned with electron-beam lithography followed by deposition of Ti/Au and liftoff. A 250 nm silicon nitride AR coating is then deposited with PECVD. Contact vias are patterned with optical lithography and etched via dry plasma etching. Finally, the logarithmic spiral antennas and bias lines are patterned again with optical lithography, followed by deposition of Ti/Au and liftoff. The fabricated plasmonic photomixers are then mounted on a hyper-hemispherical silicon lens to improve the THz radiation collection.

References:

- [1] A. M. Turing, The chemical basis of morphogenesis, *Phil. Trans. Royal Soc. London* **237**, 37 (1952).
- [2] S. Kondo and T. Miura, Reaction-diffusion model as a framework for understanding biological pattern formation, *Science* **329**, 1616 (2010).
- [3] A. Liehr, *Dissipative solitons in reaction diffusion systems: Mechanisms, dynamics, interactions*, Springer series in Synergetics, New York, New York (2013).
- [4] L. A. Lugiato and R. Lefever, Spatial dissipative structures in passive optical systems, *Phys. Rev. Lett.* **58**, 2209 (1987).
- [5] A. J. Scroggie, W. J. Firth, G. S. McDonald, M. Tlidi, R. Lefever, and L. A. Lugiato, Pattern formation in a passive Kerr cavity, *Chaos Solitons Fractals* **4**, 1323 (1994).

- [6] C. Godey, I. V. Balakireva, A. Coillet, and Y. K. Chembo, Stability analysis of the spatiotemporal Lugiato-Lefever model for Kerr optical frequency combs in the anomalous and normal dispersion regimes, *Phys. Rev. A* **89**, 063814 (2014).
- [7] A. Coillet, I. Balakireva, R. Henriet, K. Saleh, L. Larger, J. M. Dudley, C. R. Menyuk, and Y. K. Chembo, Azimuthal Turing patterns, bright and dark cavity solitons in Kerr combs generated with whispering-gallery-mode resonators, *IEEE Photon. J.* **5**, 6100409 (2013).
- [8] A. B. Matsko, W. Liang, A. A. Savchenkov, and L. Maleki, Chaotic dynamics of frequency combs generated with continuously pumped nonlinear microresonators, *Opt. Lett.* **38**, 525 (2013).
- [9] A. Coillet and Y. K. Chembo, Routes to spatiotemporal chaos in Kerr optical frequency combs, *Chaos* **24**, 013113 (2014).
- [10] T. Herr, V. Brasch, J. D. Jost, C. Y. Wang, N. M. Kondratiev, M. L. Gorodetsky, and T. J. Kippenberg, Temporal solitons in optical microresonators, *Nat. Photon.* **8**, **145** (2014).
- [11] S.-W. Huang, J. F. McMillan, J. Yang, A. Matsko, H. Zhou, M. Yu, D.-L. Kwong, L. Maleki, and C. W. Wong, Mode-locking ultrashort pulse generation from on-chip normal dispersion microresonators, *Phys. Rev. Lett.* **114**, 053901 (2015).
- [12] X. Xue, Y. Xuan, Y. Liu, P.-H. Wang, S. Chen, J. Wang, D. E. Leaird, M. Qi, and A. M. Weiner, Mode-locked dark pulse Kerr combs in normal-dispersion microresonators, *Nat. Photon.* **9**, 594 (2015).
- [13] X. Yi, Q.-F. Yang, K. Y. Yang, M.-G. Suh, and K. Vahala, Soliton frequency comb at microwave rates in a high-Q silica microresonator, *Optica* **2**, 1078 (2015).
- [14] C. Joshi, J. K. Jang, K. Luke, X. Ji, S. A. Miller, A. Klenner, Y. Okawachi, M. Lipson, and A. L. Gaeta, Thermally controlled comb generation and soliton modelocking in microresonators, *Opt. Lett.* **41**, 2565 (2016).
- [15] J. Pfeifle, A. Coillet, R. Henriet, K. Saleh, P. Schindler, C. Weimann, W. Freude, I. V. Balakireva, L. Larger, C. Koos, and Y. K. Chembo, Optimally coherent Kerr combs generated with crystalline whispering gallery mode resonators for ultrahigh capacity fiber communications, *Phys. Rev. Lett.* **114**, 093902 (2015).
- [16] Y. K. Chembo, D. V. Strekalov, and N. Yu, Spectrum and dynamics of optical frequency combs generated with monolithic whispering gallery mode resonators, *Phys. Rev. Lett.* **104**, 103902 (2010).
- [17] T. Herr, K. Hartinger, J. Riemensberger, C. Y. Wang, E. Gavartin, R. Holzwarth, M. L. Gorodetsky, and T. J. Kippenberg, Universal formation dynamics and noise of Kerr-frequency combs in microresonators, *Nat. Photon.* **6**, 480 (2012).
- [18] M. R. E. Lamont, Y. Okawachi, and A. L. Gaeta, Route to stabilized ultrabroadband microresonator-based frequency combs, *Opt. Lett.* **38**, 3478 (2013).

- [19] T. J. Kippenberg, R. Holzwarth, and S. A. Diddams, Microresonator-based optical frequency combs, *Science* **332**, 555 (2011).
- [20] S.-W. Huang, J. Yang, M. Yu, B. H. McGuyer, D.-L. Kwong, T. Zelevinsky, and C. W. Wong, A broadband chip-scale optical frequency synthesizer at 2.7×10^{-16} relative inaccuracy, *Sci. Adv.* **2**, e1501489 (2016).
- [21] P. Del'Haye, A. Coillet, T. Fortier, K. Beha, D. C. Cole, K. Y. Yang, H. Lee, K. J. Vahala, S. B. Papp, and S. A. Diddams, Phase-coherent microwave-to-optical link with a self-referenced microcomb, *Nat. Photon.* **10**, 516 (2016).
- [22] A. A. Savchenkov, A. B. Matsko, W. Liang, V. S. Ilchenko, D. Seidel, and L. Maleki, Kerr frequency comb generation in overmoded resonators, *Opt. Express* **20**, 27290 (2012).
- [23] I. S. Grudinin, L. Baumgartel, and N. Yu, Impact of cavity spectrum on span in microresonator frequency combs, *Opt. Express* **21**, 26929 (2013).
- [24] Y. Liu, Y. Xuan, X. Xue, P.-H. Wang, S. Chen, A. J. Metcalf, J. Wang, D. E. Leaird, M. Qi, and A. M. Weiner, Investigation of mode coupling in normal-dispersion silicon nitride microresonators for Kerr frequency comb generation, *Optica* **1**, 137 (2014).
- [25] S.-W. Huang, J. Yang, J. Lim, H. Zhou, M. Yu, D.-L. Kwong, and C. W. Wong, A low-phase-noise 18 GHz Kerr frequency microcomb phase-locked over 65 THz, *Sci. Rep.* **5**, 13355 (2015).
- [26] K. Unterrainer, A. Benz, J. Darmo, C. Deutsch, G. Fasching, J. Kröll, D. P. Kelly, M. Marth, T. Müller, W. Parz, S. S. Dhillon, C. Sirtori, A. M. Andrews, W. Schrenk, G. Strasser, X. Marcadet, M. Calligaro, H. E. Beere, and D. A. Ritchie, Terahertz quantum cascade devices: from intersubband transition to microcavity laser, *IEEE J. Sel. Top. Quant. El.* **14**, 307 (2008).
- [27] S. Jung, A. Jiang, Y. Jiang, K. Vijayraghavan, X. Wang, M. Troccoli, and M. A. Belkin, Broadly tunable monolithic room-temperature terahertz quantum cascade laser sources, *Nat. Commun.* **5**, 4267 (2014).
- [28] C. Sirtori, S. Barbieri, and R. Colombelli, Wave engineering with THz quantum cascade lasers, *Nat. Photon.* **7**, 691 (2013).
- [29] J. Darmo, V. Tamosiunas, G. Fasching, J. Kröll, and K. Unterrainer, Imaging with a terahertz quantum cascade laser, *Opt. Express* **12**, 1879 (2004).
- [30] S. Koenig, D. Lopez-Diaz, J. Antes, F. Boes, R. Henneberger, A. Leuther, A. Tessmann, R. Schmogrow, D. Hillerkuss, R. Palmer, T. Zwick, C. Koos, W. Freude, O. Ambacher, J. Leuthold, and I. Kallfass, Wireless sub-THz communication system with high data rate, *Nat. Photon.* **7**, 977 (2013).
- [31] C. W. Berry, M. R. Hashemi, S. Preu, H. Lu, A. C. Gossard, and M. Jarrahi, High power terahertz generation using 1550 nm plasmonic photomixers, *Appl. Phys. Lett.* **105**, 011121 (2014).

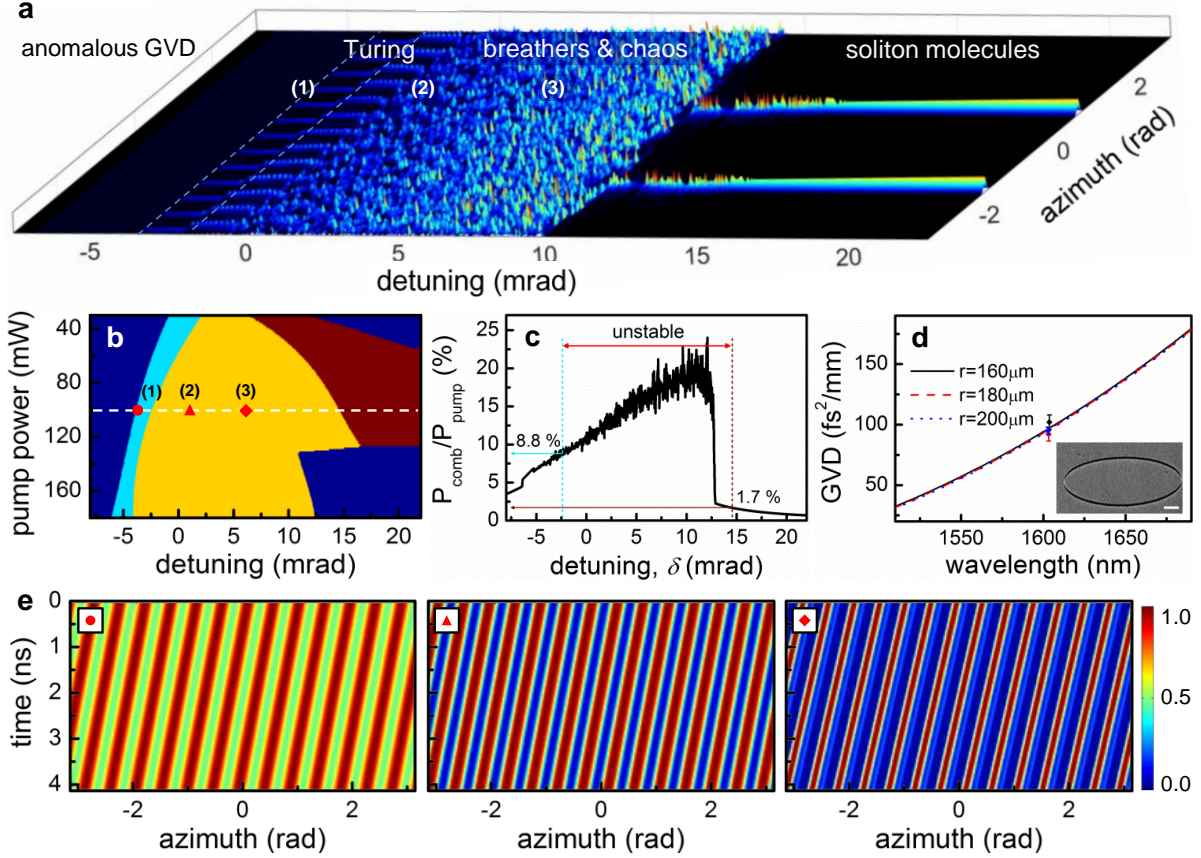


Figure 1. (a) Evolution dynamics along the white dashed line in (b) at 100 mW on-chip pump power. Spontaneous Turing pattern is formed, then collapsed into breather states, destabilized into chaos, and eventually transformed into soliton molecules with a proper scan protocol of pump detuning. (b) Stability diagram of the Turing pattern. Light blue: region of stable spontaneous Turing pattern; yellow: region of breathers and spatiotemporal chaos; red: region of soliton and soliton molecules. (c) Pump-to-comb power conversion efficiency along the white dashed line in (b), showing only 8.8% and 1.7% maximum power conversions to Turing pattern and soliton molecules respectively. (d) Group velocity dispersion (GVD) of our ring resonators, featuring large normal GVDs of +100 fs²/mm. The ring radius is designed to be large enough (more than 160 μm) such that the bending-induced dispersion is negligible. Measured GVDs at 1603 nm (circles with error bars) show good agreements with the numerical modeling. Inset: scanning electron micrograph of the nonlinear ring resonator. Scale bar: 50 μm. (e) Universally stable Turing pattern formation across a large detuning range from -77 MHz to 154 MHz, through local mode hybridization to satisfy the phase matching condition. The detuning points with the hybridized mode dispersion [red circle, triangle, and diamond] are overlaid onto the reference map (originally with anomalous GVD), for comparison. Symmetry breaking in the Turing pattern spectrum (Figure S1) leads to either acceleration or deceleration of the Turing roll, resulting in the tilt with respect to the time axis.

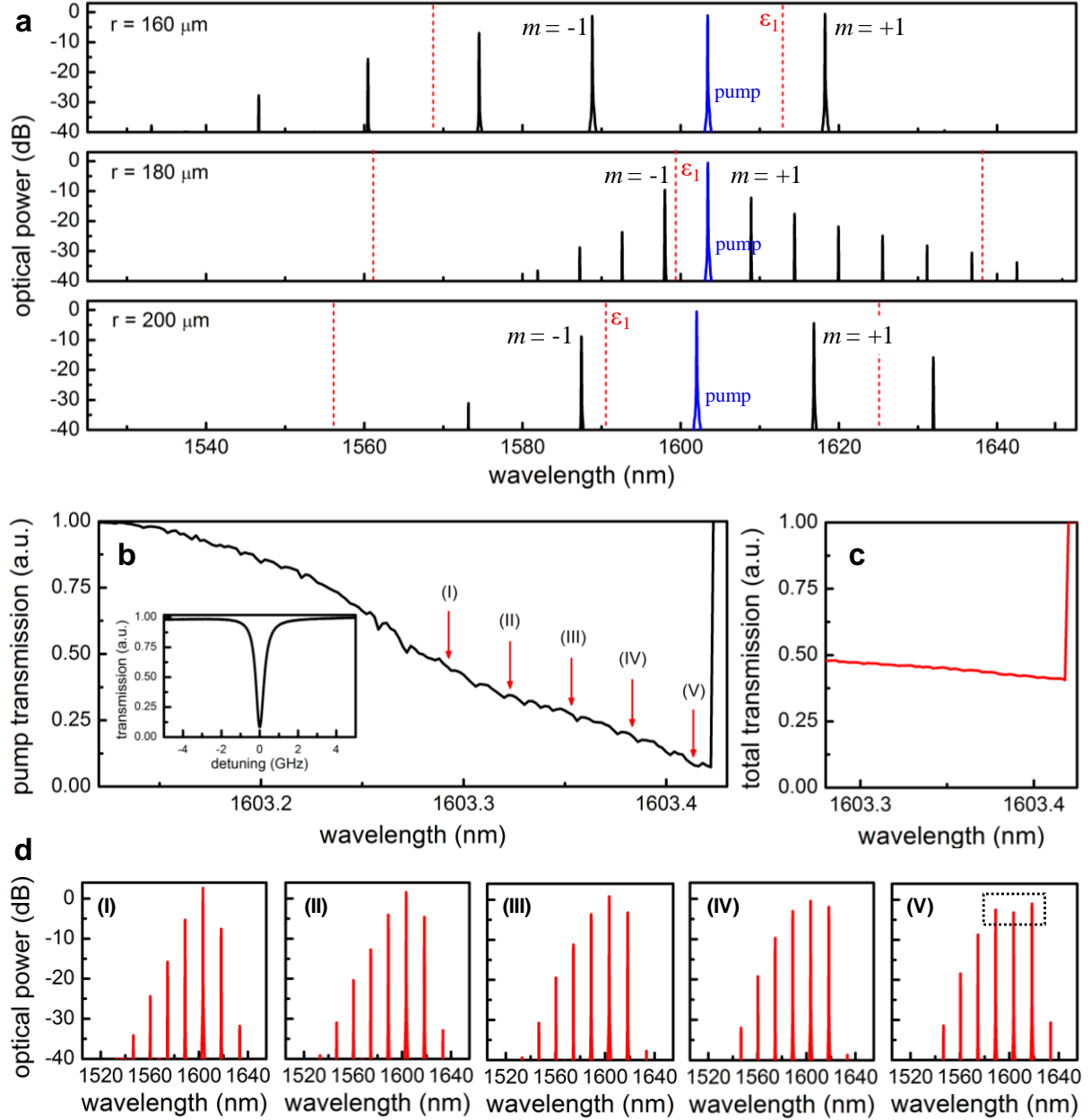


Figure 2. (a) Turing rolls generated from ring resonators with different radii. Even though the group velocity dispersion of the ring resonators differ by less than $2 \text{ fs}^2/\text{mm}$, the TM_{11} - TM_{21} mode hybridization positions (red dashed lines) with respect to the pump (blue lines) shift due to the change in the ring radii, resulting in abrupt dispersion variations locally and very different spontaneous Turing patterns. The Turing roll repetition rates are 1.72 THz ($12 \times \text{FSR}$) for the $160 \mu\text{m}$ radius ring, 0.64 THz ($5 \times \text{FSR}$) for the $180 \mu\text{m}$ radius ring, and 1.72 THz ($15 \times \text{FSR}$) for the $200 \mu\text{m}$ radius ring. (b) Pump-cavity transmission as a function of the pump wavelength, labeling the detunings where different Turing roll stages are generated. Inset: The cold resonance of the pump mode, measuring a loaded Lorentzian linewidth of 500 MHz and a loaded quality factor of 3.7×10^5 . (c) Total cavity transmission as a function of the pump wavelength in the

range where Turing roll is generated. Compared to the pump-cavity transmission, the total cavity transmission shows a less apparent decrease as the pump is tuned into the resonance, indicating an efficient power conversion from the pump to the generated Turing lines. **(d)** Example Turing roll spectra at different stages. At stage V, even a highly depleted pump close to the resonance is observed in the measurement, illustrated in the dashed box.

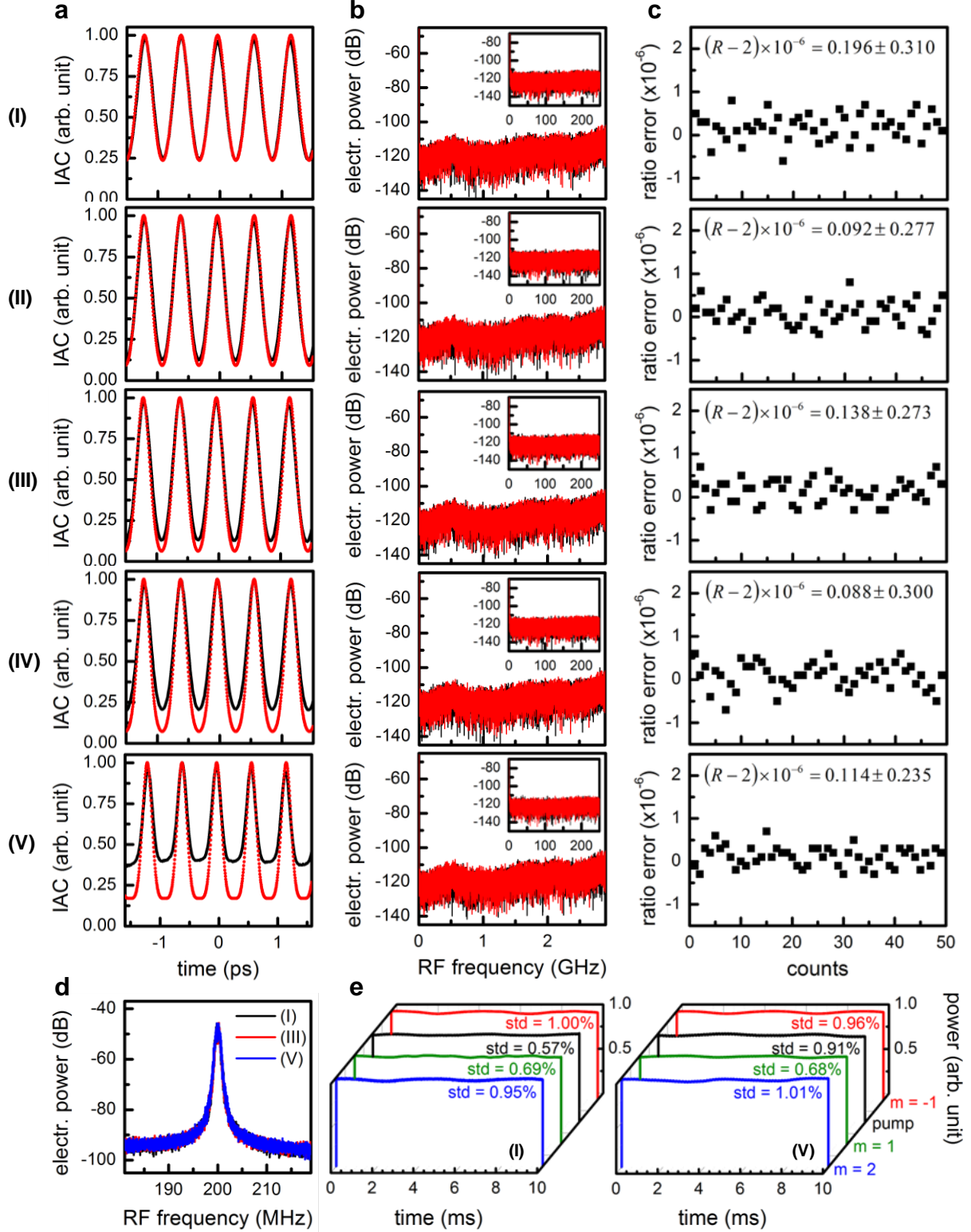


Figure 3. (a) Intensity autocorrelation (IAC) traces of the Turing rolls at different stages. The red dashed lines are the ideal traces calculated from the spectra, while the black curves are the measured traces. As the sidebands grow, the deviations between the measured and calculated

IAC traces also increase. **(b)** To examine the emergence of incommensurate sub-combs, RF amplitude noise spectra of the Turing rolls (black curve) along with the detector background (red curve) are measured up to 3 GHz, six times the cavity linewidth. No apparent amplitude noise is observed, verifying the existence of the commensurate sub-combs. Inset: zoom-in RF amplitude noise spectra up to 250 MHz, at the instrumentation detection noise floor. **(c)** To probe the equidistance of the Turing rolls, the beat notes between the three Turing roll sidebands (pump, $m = 1$, and $m = 2$) and the adjacent fiber laser frequency comb lines are measured and the ratio errors are presented. The small deviation from the ideal ratio R of 2 [R defined in the main text as $(\delta_2 - \delta_0)/(\delta_1 - \delta_0)$] verifies Turing pattern's excellent uniformity. The average non-uniformity is measured at 125 mHz, or 6.6×10^{-16} when referenced to the optical carrier. **(d)** The linewidth of the 1st sideband is measured at 500 kHz, limited by the coherence of the pump laser, by the self-heterodyne technique at different stages. No linewidth broadening is observed, independently confirming that the coherence of the Turing roll is maintained at all evolving stages. **(e)** Power fluctuation of individual sidebands at the stages I (left) and V (right) with a sampling rate of 250 MHz, ruling out the possibility of breathing solutions.

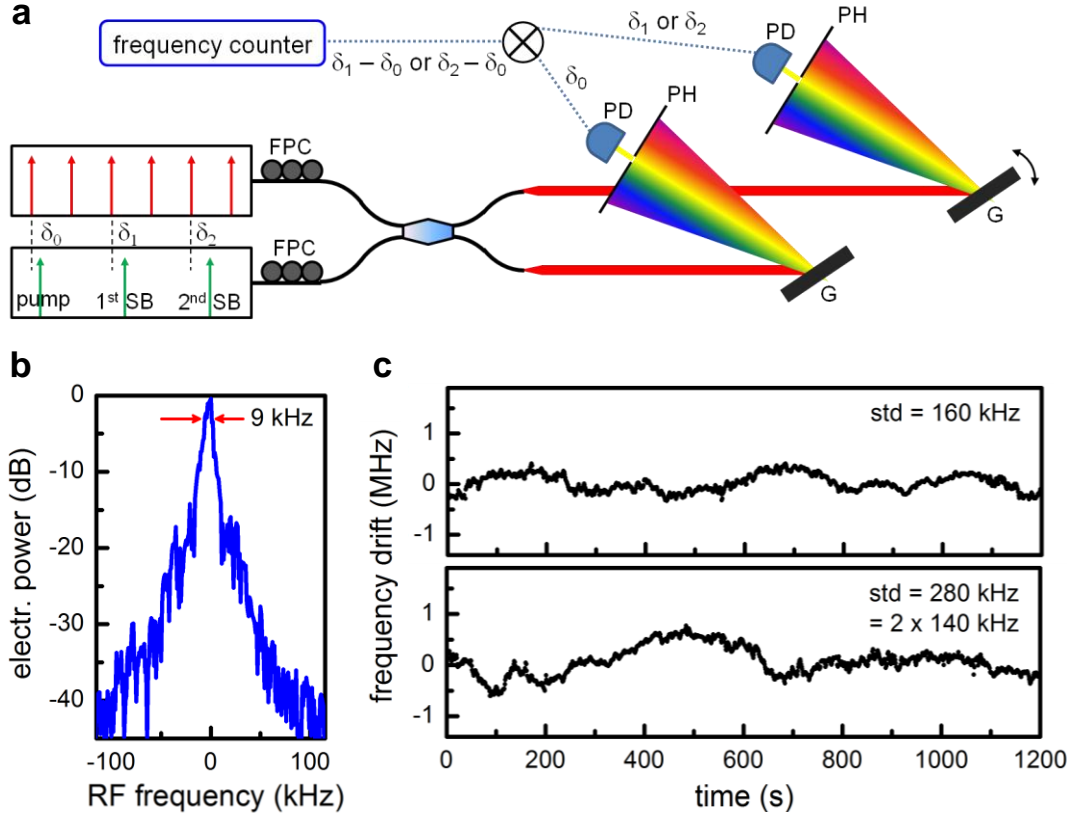


Figure 4. (a) To characterize the repetition rate drift of the Turing roll (shown as the green arrows), beat notes by mixing the pump and the sidebands with the adjacent fiber laser frequency comb lines are measured. The difference between the two beat notes, a measure of the repetition rate drift, is counted with a gate time of 1 s. (b) On a 200 ms scale, the measured beat note has a FWHM linewidth of 9 kHz, on a measurement resolution bandwidth of 3 kHz. (c) Top: Long term frequency drift of the 1st sideband with respect to the pump, showing the repetition rate drift of 160 kHz over 20 minutes. Bottom: Long term frequency drift of the 2nd sideband with respect to the pump, showing a consistent repetition rate drift of 140 kHz.

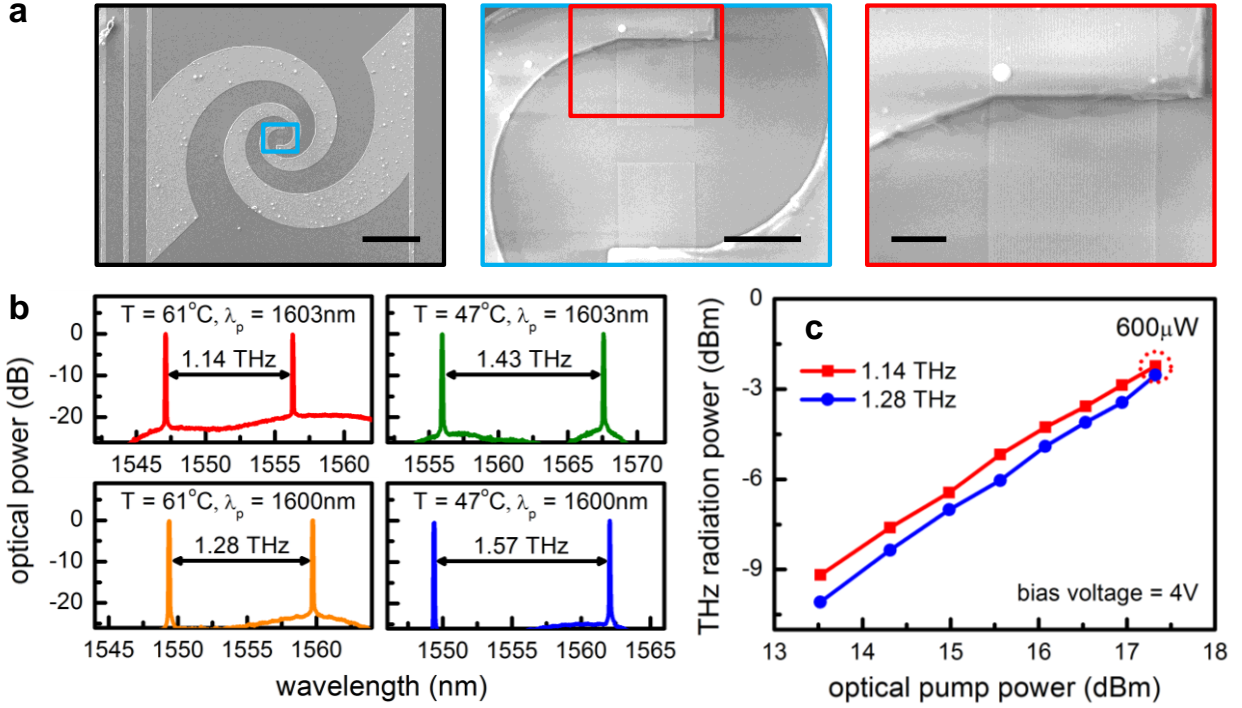


Figure 5. (a) Scanning electron micrographs of the fabricated plasmonic photomixer with a logarithmic spiral antenna integrated with plasmonic contact electrodes on an ErAs:InGaAs substrate. Scale bars from left to right: 100 μm , 10 μm , and 3 μm . (b) Turing roll repetition rate, and hence the generated THz frequency, can be tuned by changing the pump wavelength and the resonator temperature. (c) THz radiation power as a function of optical pump power. Power conversion efficiency of 1.1 % can be obtained with an optical pump power of 54 mW.

Supplemental Material for

Universally stable microresonator Turing pattern formation for coherent high-power THz radiation on-chip

Shu-Wei Huang^{1,*}, Jinghui Yang¹, Shang-Hua Yang², Mingbin Yu³, Dim-Lee Kwong³, T. Zelevinsky⁴, Mona Jarrahi², and Chee Wei Wong^{1,*}

¹ Fang Lu Mesoscopic Optics and Quantum Electronics Laboratory, University of California, Los Angeles, CA 90095, USA.

² Terahertz Electronics Laboratory, University of California, Los Angeles, CA 90095, USA.

³ Institute of Microelectronics, A*STAR, Singapore 117865, Singapore.

⁴ Department of Physics, Columbia University, New York, NY 10027, USA.

* Author e-mail address: swhuang@seas.ucla.edu ; cheewei.wong@ucla.edu

I. Spontaneous Turing pattern formation through modelled Lugiato-Lefever dynamics

In our model we numerically studied the Turing roll formation using the Lugiato-Lefever equation (LLE), $T_R \frac{\partial}{\partial t} A(t, \tau) = \sqrt{\alpha_c} A_{in} - \left[\frac{\alpha_c + \alpha_p}{2} + j\delta + j\bar{D}L + j \frac{n_2 \omega_L}{c} I(t, \tau) \right] A(t, \tau)$, for its computational efficiency [S1]. Here α_p is the propagation loss, α_c is the coupling loss, δ is the detuning, and $\bar{D} = \sum_{n \geq 2} \frac{\beta_n}{n!} \left(-j \frac{\partial}{\partial \tau} \right)^n$ is the dispersion operator. The LLE was solved for 2,001 modes around the cw pump. The simulation started from vacuum noise and was run for 10^6 roundtrips until the solutions reached the steady state.

In the anomalous dispersion regime (top panel of Figure S1), a spontaneous growth of symmetric Turing roll was observed. As the wavelength was tuned closer to resonance, sub-comb started to emerge and destabilize the Turing pattern. On the other hand, growth of Turing roll is prohibited in the normal dispersion regime unless local dispersion disruption by mode hybridization is introduced (bottom panel of Figure S1). To account for the local dispersion disruption, we artificially changed the resonance frequency of the -14th mode such that $2\omega_0 - \omega_{14} - \omega_{-14}$ is phase matched. Then a spontaneous growth of Turing pattern was observed, but clearly the spectral symmetry was broken. Furthermore, sub-comb growth and transition into chaos were forbidden.

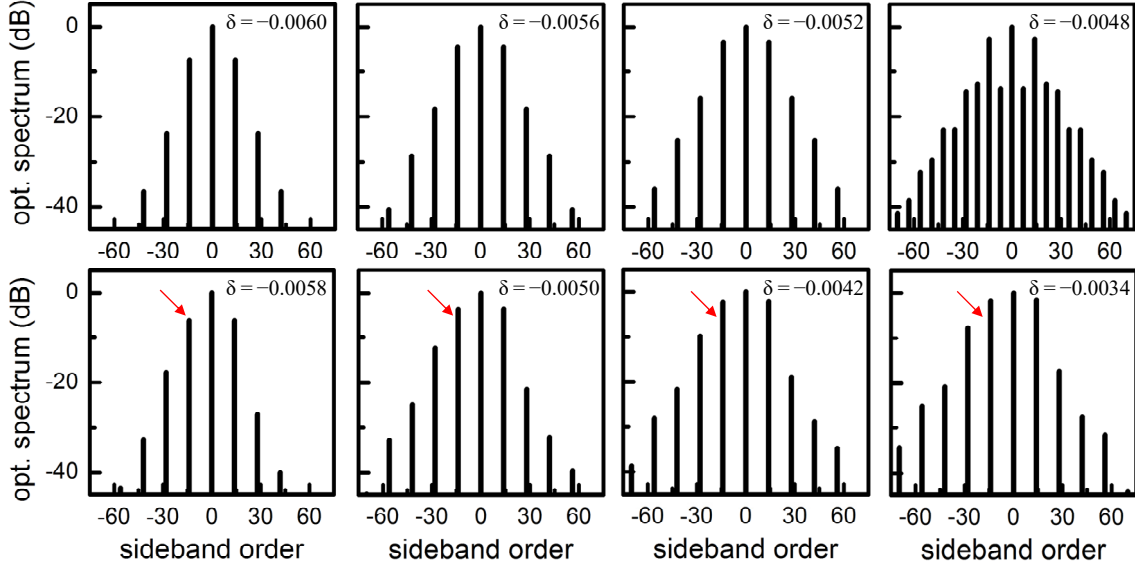


Figure S1 | Lugiato-Lefever modeling of the spontaneous Turing pattern formation. Top: Simulation with anomalous group delay dispersion (-1300 fs^2), showing a spontaneous growth of Turing rolls. Bottom: Simulation of the Turing roll in the normal dispersion microresonator (1300 fs^2), where the Turing roll is excited by local mode hybridization. It shows an apparent asymmetry and can be tuned further into resonance without triggering the sub-comb growth. The red arrow points to the mode where local dispersion disruption is introduced in the Lugiato-Lefever model.

II. Turing rolls for coherent high-power tunable THz generation

Figure S2 shows the intensity autocorrelation (IAC) profile of the Turing roll at the stage III. Due to the efficient energy conversion from the pump to the first sideband pair, the Turing roll features a quasi-sinusoidal intensity profile with a negligible background of less than 1% of the peak intensity. Nearly background-free operation is important for efficient on-chip THz generation as it reduces the risk of thermal breakdown.

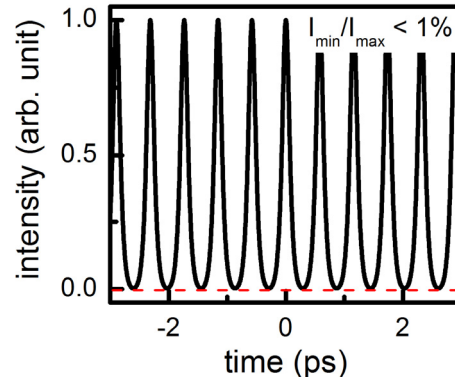


Figure S2 | Measured intensity profile of the sub-picosecond Turing roll, showing a quasi-sinusoidal oscillation with a more than 100 contrast.

III. Temporal dynamics of the tunable Turing pattern formation

To probe the robustness of the Turing pattern formation to the perturbations in initial conditions and pump wavelength tuning speeds, we recorded IAC traces of the Turing rolls generated under three different tuning speeds on two different days. The results are summarized in Figure S3. Unlike the microresonator soliton generation where the initial condition and the tuning speed play key roles in determination of the soliton states, here the Turing roll always evolves in the identical route and is robust against perturbations in initial conditions and pump wavelength tuning speeds.

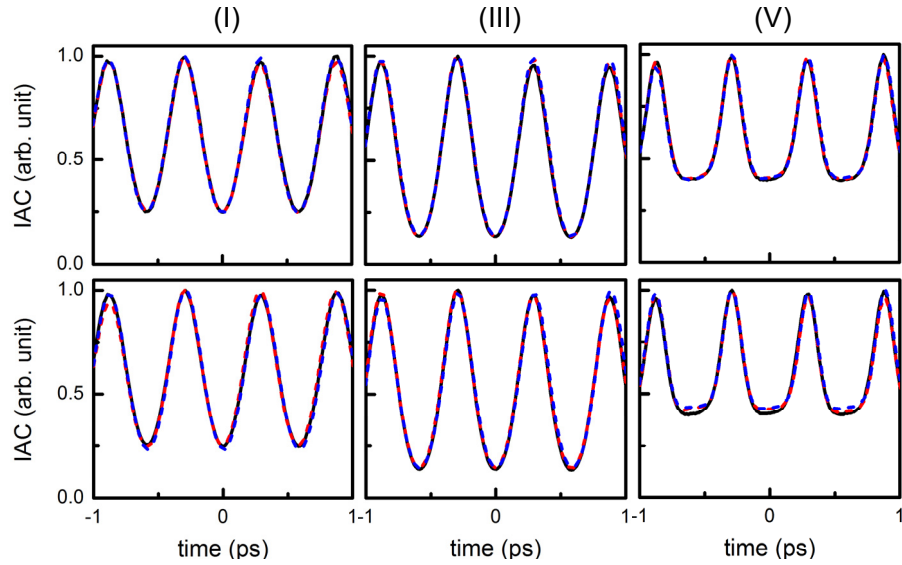


Figure S3 | At three different scanning speeds (black curve: 1 nm/s; red dashed curve: 0.3 nm/s; blue dashed curve: 0.1 nm/s) and two independent starts (top and bottom), the Turing roll shows the identical generation route.

Figure S4 illustrates how applying an additional dispersion (30 cm SMF28) leads to different temporal structure changes of the Turing pattern at two example detunings. The effect can be understood as the consequence of the pump phase slip around the resonance. As shown in Figure S5a, the output pump will experience a π phase shift as it traverses through the resonance. Such phase slip is due to the interference between the intracavity and the input pump and thus the other sidebands of the Turing roll will not experience such a phase shift. This additional pump phase slip results in the observed change of temporal structure. The distinct responses to dispersion illustrated in Figure S4 are well captured by considering the pump phase offset (Figure S5). Of note, most of the phase slip happens very close to cavity resonance and thus the observation of its effect is attributed to the unique design of our microresonator, which utilizes

the local mode hybridization to fulfill the phase matching of spontaneous Turing pattern formation and greatly suppresses the Turing pattern destabilization even when the pump is deep into the resonance.

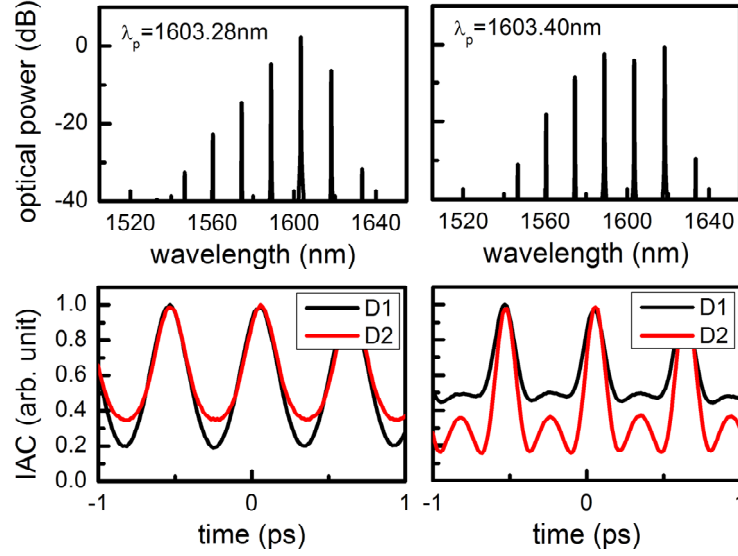


Figure S4 | IAC traces of the Turing rolls at two different pump detunings ($\lambda_p = 1603.28 \text{ nm}$ and $\lambda_p = 1603.40 \text{ nm}$) with two external dispersion compensation. Here D1 and D2 use 60 cm and 90 cm SMF-28 fibers as the external dispersion elements, respectively.

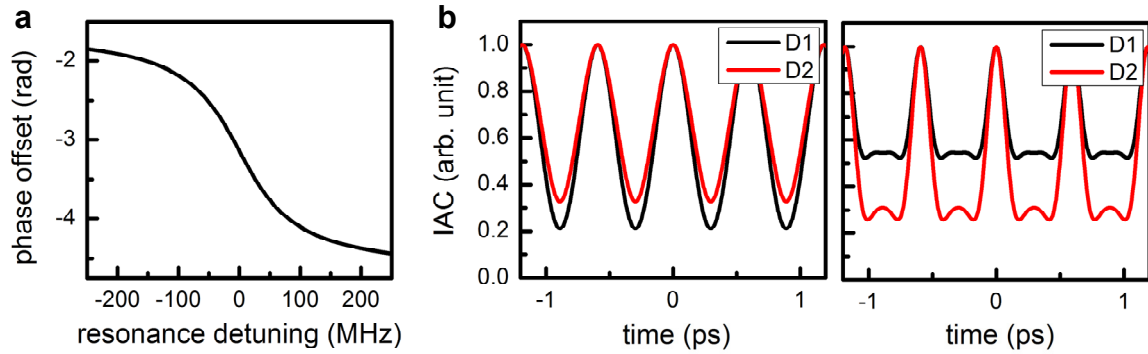


Figure S5 | (a) Phase offset between the intracavity and output pump light, showing a π phase slip around the resonance. (b) IAC traces calculated by adding $\pi/2$ to the pump wavelength for $\lambda_p = 1603.40 \text{ nm}$, showing a good agreement with the measurements shown in Figure S4.

IV. Spontaneous Turing pattern measurement setup schematics

Figure S6 shows the schematic diagram of the dispersion measurement setup [S4]. The microresonator transmission was recorded when the laser was swept from 1550 nm to 1630 nm at a tuning speed of 40 nm/s. The sampling clock of the data acquisition is derived from the photodetector monitoring the laser transmission through a fiber Mach-Zehnder interferometer

with 40 m unbalanced path lengths, which translates to a 5 MHz optical frequency sampling resolution. Transmission of the hydrogen cyanide gas cell was simultaneously measured and the absorption features were used for absolute wavelength calibration. Each resonance was fitted with a Lorentzian lineshape to determine the resonance frequency and the quality factor. The microresonator dispersion was then calculated by analyzing the wavelength dependence of the free spectral range.

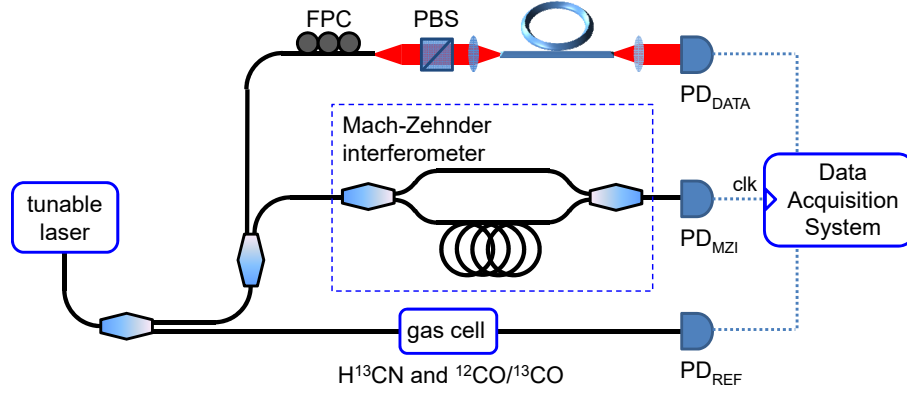


Figure S6 | Turing microresonator dispersion measurement setup.

Figure S7 shows the schematic diagram of the uniformity measurement setup to probe the equidistance of the Turing roll sidebands. The generated Turing roll was split and sent to 3 beat detection units (BDUs) individually optimized for the wavelength of the pump (1603 nm), the 1st sideband (1589 nm), and the 2nd sideband (1575 nm). Heterodyne beat notes were generated between the Turing roll (green arrows) and a reference fiber laser frequency comb (red arrows). The gratings in the BDUs critically suppress the unwanted reference fiber laser frequency comb teeth such that clean heterodyne beat notes with more than 40 dB signal to noise ratio (measured with a 100 kHz resolution bandwidth), sufficient for reliable measurements, can be routinely obtained. The beat notes from the sidebands (δ_1 and δ_2) were mixed with the beat note from the pump (δ_0) to cancel the residual pump wavelength instability before being measured by a high-resolution frequency counter (10 mHz frequency error at 1 second). The frequency counter was operated in the ratio counting mode, to circumvent the synchronization challenge of simultaneous beat note measurements and achieve a more accurate measurement.

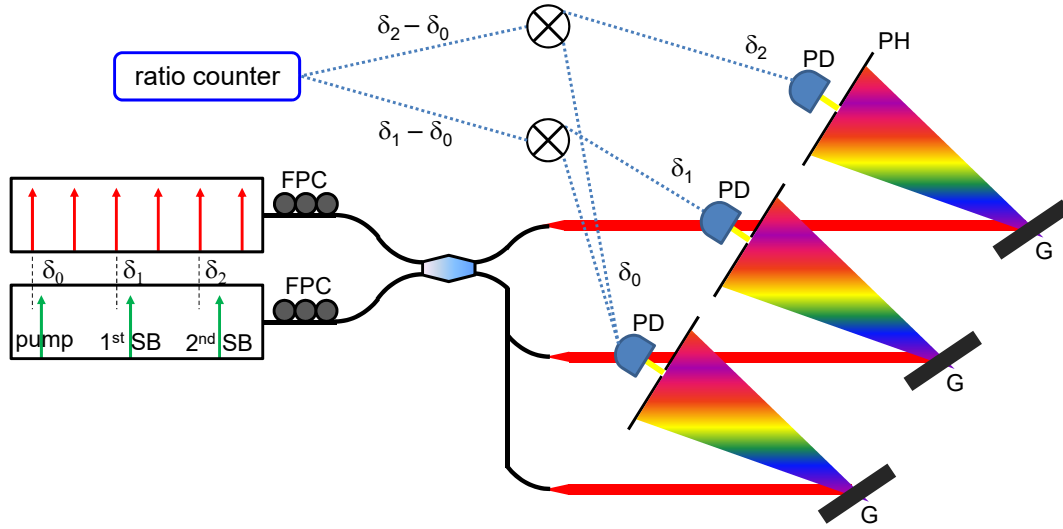


Figure S7 | Turing pattern sideband frequency uniformity measurement setup.

Figure S8 shows the schematic diagram of the self-heterodyne linewidth measurement setup [S5]. The input was split into two parts with 70% of it being sent through an acousto-optic modulator which shifts the optical frequencies by 200 MHz. The other portion was sent through a 5 km single mode optical fiber, providing a time delay of 24.5 μ s. Both lights were then recombined, and the resulting beat note was recorded and analyzed with a high-speed photodetector and an electrical spectrum analyzer. The RF spectrum becomes a self-convolution of the laser spectrum, from which the linewidth can be retrieved, as long as the coherence length is shorter than the introduced delay. Thus our self-heterodyne measurement setup can measure a minimum linewidth at 13 kHz, about 40 times smaller than the measured laser linewidth.

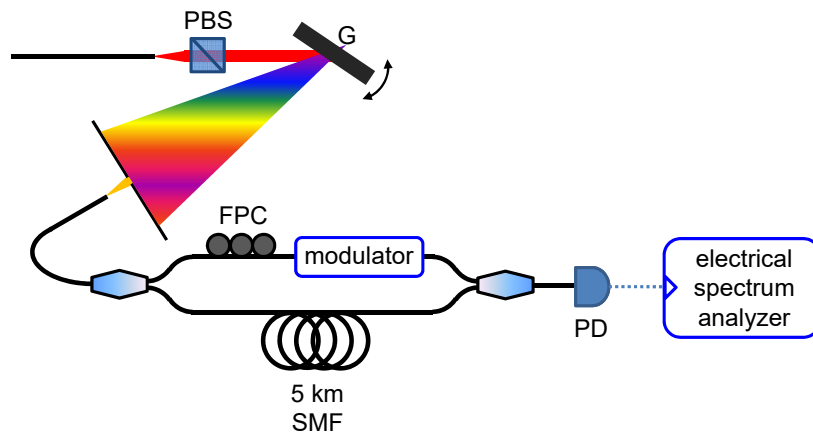


Figure S8 | Self-heterodyne measurement setup.

Figure S9 shows the schematic diagram of the THz radiation generation setup. A C/L WDM filter, followed by an erbium doped fiber amplifier (EDFA), was used to selectively amplify the Turing roll sidebands in the 1530 to 1565 nm C-band range. A 500 kHz intensity modulator was utilized to reduce the duty cycle of the Turing roll to 1%, thereby increasing the thermal breakdown onset threshold. Efficient photomixing [S2] is achieved based on a logarithmic spiral plasmonic antenna design [S3] for efficient THz radiation generation. To achieve the highest photomixing efficiency, both the focus spot size and the position of the optical pump were adjusted to maximize the induced photocurrent level. The generated THz radiation was then measured with a liquid helium-cooled silicon bolometer. Lock-in detection technique was implemented to reduce the noise level and obtain a more reliable reading of the THz radiation power.

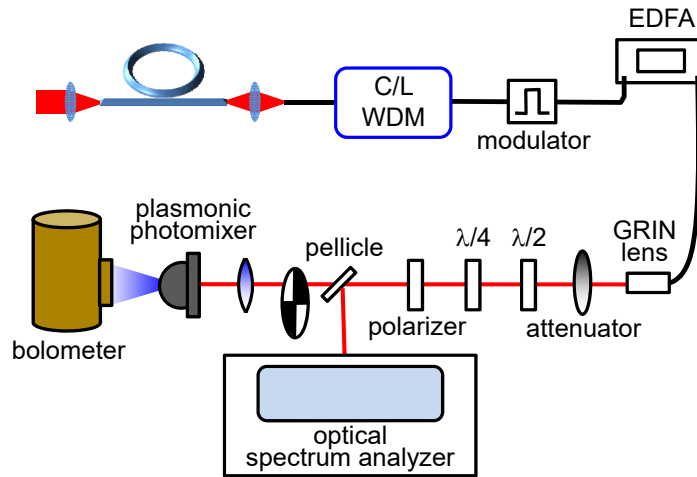


Figure S9 | THz radiation generation setup.

Supplemental References:

- [S1] S. Coen, H. G. Randle, T. Sylvestre, and M. Erkintalo, Modeling of octave-spanning Kerr frequency combs using a generalized mean-field Lugiato–Lefever model, *Opt. Lett.* **38**, 37 (2013).
- [S2] H. Tanoto, J. H. Teng, Q. Y. Wu, M. Sun, Z. N. Chen, S. A. Maier, B. Wang, C. C. Chum, G. Y. Si, A. J. Danner, and S. J. Chua, Nano-antenna in a photoconductive photomixer for highly efficient continuous wave terahertz emission, *Sci. Rep.* **3**, 2824 (2013).
- [S3] C. W. Berry, M. R. Hashemi, S. Preu, H. Lu, A. C. Gossard, and M. Jarrahi, High power terahertz generation using 1550 nm plasmonic photomixers, *Appl. Phys. Lett.* **105**, 011121 (2014).

[S4] S.-W. Huang, H. Zhou, J. Yang, J. F. McMillan, A. Matsko, M. Yu, D.-L. Kwong, L. Maleki, and C. W. Wong, Mode-Locked Ultrashort Pulse Generation from On-Chip Normal Dispersion Microresonators, *Phys. Rev. Lett.* **114**, 053901 (2015).

[S5] T. Okoshi, K. Kikuchi, and A. Nakayama, Novel method for high resolution measurement of laser output spectrum, *Electron. Lett.* **16**, 630 (1980).